Ceramics International 44 (2018) 4883–4890

Contents lists available at ScienceDirect

Ceramics International

journal homepage: www.elsevier.com/locate/ceramint

Barnacle-like manganese oxide decorated porous carbon nanofibers for high-performance asymmetric supercapacitors

Dong-Yo Shin[a], Geon-Hyoung An[a], Hyo-Jin Ahn[a,b,*]

[a] Program of Materials Science & Engineering, Convergence Institute of Biomedical Engineering and Biomaterials, Seoul National University of Science and Technology, Seoul 01811, Republic of Korea

[b] Department of Materials Science and Engineering, Seoul National University of Science and Technology, Seoul 01811, Republic of Korea

ARTICLE INFO

Keywords:
Capacitor
Composites
Carbon
Fibres
Surfaces
Manganese oxide

ABSTRACT

In this study, barnacle-like manganese oxide (MnO_2) decorated porous carbon nanofibers (PCNF) were synthesized using electrospinning and the chemical precipitation method for high-performance asymmetric supercapacitors. The porous structure of PCNF was acquired using poly(styrene-*co*-acrylonitrile) in the electrospinning solution. In order to obtain the optimized barnacle-like MnO_2 on PCNF (MnO_2-PCNF), the barnacle-like MnO_2 was synthesized using different synthetic times (namely, 1.5, 3.0, and 7.0 min) of the chemical precipitation. Among them, the optimized MnO_2-PCNF for 3.0 min exhibited the well-dispersed MnO_2 on the PCNF with the nano-size of 190–218 nm. The optimized MnO_2-PCNF showed the superior specific capacitance of 209.8 F g^{-1} at 10 mV s^{-1} and the excellent high-rate performance of 160.3 F g^{-1} at 200 mV s^{-1} with the capacitance retention of 98.7% at 100 mV s^{-1} for 300 cycles. In addition, electrochemical performances of asymmetric cell (constructed activated carbon and MnO_2-PCNF) showed the high specific capacitance of 60.6 F g^{-1} at the current density of 0.5 A g^{-1}, high-rate capacitance of 30.0 F g^{-1} at the current density of 10 A g^{-1}, and the excellent energy density of 30.3–15.0 Wh kg^{-1} in the power density range from 270 to 9000 W kg^{-1}. The enhanced electrochemical performance can be explained by the synergistic effects of barnacle-like MnO_2 nanoparticles with a high active area related to high specific capacitance and well-dispersed MnO_2 with a short ion diffusion length related to the excellent high-rate performance.

1. Introduction

In recent years, due to the characteristics of high power density, excellent cycling stability, fast energy-storage ability, and low operating temperature, electrochemical capacitors (ECs) have started to be widely used for various applications such as electric vehicles, portable electronic devices, and industrial power management [1–4]. In general, ECs are categorized into electric double-layer capacitors (EDLCs) and pseudo-capacitors (PCs) by different energy-storage mechanisms [5–7]. The principle of EDLCs is based on the physical adsorption of electrostatic charges in electrical double-layer between the electrode and the electrolyte. The principle of PCs is based on the chemical reaction with the faradaic redox reaction between the electrode and electrolyte. As compared to EDLCs, PCs have the attractive advantage of a higher energy density. Furthermore, PCs are composed of an electrode, an electrolyte, and a separator. Among those, electrode material is directly related to high-performance PCs that are commonly used for transition-metal oxides, such as manganese oxide (MnO_2), nickel oxide (NiO), cobalt oxide (Co_3O_4), vanadium oxide (V_2O_5), and ruthenium oxide (RuO_2) [8–11]. Among transition-metal oxides, MnO_2 is a promising candidate as an electrode material for the high-performance PCs owing to its high theoretical specific capacitance (1380 F g^{-1}), as well as low cost, and eco-friendliness. However, despite its various advantages, MnO_2 is limited in its use as an electrode material in PCs due to the aggregation of MnO_2 and low electric conductivity, which results in a poor electrochemical performance [12–14]. To address these issues, carbon-based materials (graphite, graphene, carbon nanotubes (CNT), and carbon nanofibers (CNF)), characterized by a high electrical conductivity, a high specific surface area, and an excellent electrochemical stability, are employed as support materials for MnO_2 in PCs [15–17]. In particular, CNF is reported for support materials due to the high specific surface area (448 m^2 g^{-1}), low electrical resistivity (1.7×10^2 S m^{-1}), and superb physical/chemical stability, as well as the network structure [18–22]. The network structure consisting of one-dimensional nanofibers can afford the efficient electron transfer and a fast ion diffusion rate. For these reasons, many researchers have studied the MnO_2 and CNF composites in order to solve the above-mentioned problems. However, well-dispersed barnacle-like MnO_2 nanoparticles on porous

* Corresponding author at: Department of Materials Science and Engineering, Seoul National University of Science and Technology, Seoul 01811, Republic of Korea.
E-mail address: hjahn@seoultech.ac.kr (H.-J. Ahn).

https://doi.org/10.1016/j.ceramint.2017.12.078
Received 14 November 2017; Received in revised form 11 December 2017; Accepted 11 December 2017
Available online 12 December 2017
0272-8842/

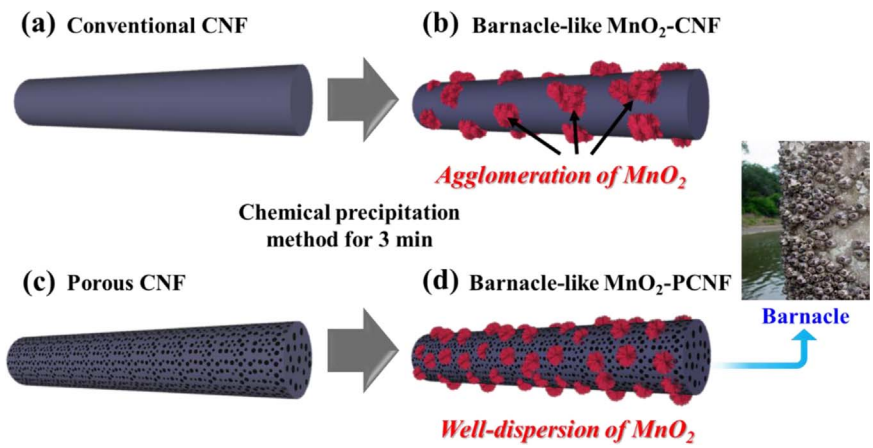

Fig. 1. A schematic illustration of (a) the conventional CNF by only the PAN polymer using electrospinning; (b) the MnO_2-CNF3 using the chemical precipitation method; (c) the PCNF by the SAN polymer using electrospinning, and (d) the MnO_2-PCNF3 using the chemical precipitation method.

carbon nanofiber (PCNF) have not yet been thoroughly studied for high-performance PCs.

Furthermore, one of key factors in an appropriate dispersion of the MnO_2 on CNF supports is development of a porous structure. The unique structure of well-dispersed MnO_2 nanoparticles on PCNF supports can lead to increase the active site and reduce the ion diffusion length for high-performance PCs. In the present study, we report synthesizing PCNF supports and well-dispersed barnacle-like MnO_2 nanoparticles on supports using electrospinning and the chemical precipitation method, and demonstrate their improved electrochemical performance.

2. Experimental

The barnacle-like MnO_2 decorated PCNFs were synthesized using an electrospinning and the chemical precipitation method. In order to synthesize the PCNFs, polyacrylonitrile (PAN, M_w = 150,000 amu, Aldrich) and poly(styrene-*co*-acrylonitrile) (SAN, M_w = 165,000 amu, Aldrich) were dissolved in N,N-dimethylformamide (DMF, 99.8%, Aldrich) under stirring for 5 h. Specifically, the SAN polymer was used for the formation of pore on the CNF supports. The electrospinning process was papered as follows. The syringe feeding rate was applied at 0.03 ml h^{-1}. The distance between the collector and the syringe needle was fixed at ~ 15 cm in the humidity of 10%. The voltage was maintained at ~ 13 kV. The as-spun nanofibers were stabilized at 280 °C for 2 h in air and then carbonized at 800 °C for 2 h in nitrogen atmosphere (99.999%). The porous structure of CNF was formed by the decomposition of the SAN polymer during the carbonization process [23]. In order to decorate the barnacle-like MnO_2 on PCNFs, PCNFs were dispersed in 2 M sulfuric acid (H_2SO_4, 95%, Aldrich) with stirring for 30 min at 80 °C, which was followed by adding potassium permanganate ($KMnO_4$, M_w = 156.03 g mol^{-1}, 99%, Aldrich) to the prepared solution. To obtain the optimized amount of MnO_2 on PCNFs, three different types of samples were prepared: 1.5, 3, and 7 min during the synthetic time of the chemical precipitation method. All samples were then washed for several times using DI-water. In what follows, the three types of samples are referred to as MnO_2-PCNF1.5, MnO_2-PCNF3, and MnO_2-PCNF7, respectively. For comparison, the barnacle-like MnO_2 decorated CNFs without the porous structure of CNF was synthesized for 3 min using the above-mentioned method (referred to herein as MnO_2-CNF3).

The structural and morphological characteristics of all samples were investigated by field emission-scanning electron microscopy (FESEM; Hitachi S-4800) and transmission electron microscopy (TEM; JEOL, 2100 F, KBSI Suncheon Center). Furthermore, X-ray diffraction (XRD, Rigaku D/MAX2500V) with Cu K_α radiation and X-ray photoelectron spectroscopy (XPS, ESCALAB250) with Al Kα X-ray source were used to investigate the crystallinity and the chemical bonding states, respectively. The electrochemical measurements were performed using a conventional three-electrode system with potentiostat/galvanostat (Autolab PGSTAT302N, FRA32M) in 0.5 M H_2SO_4 solution as the electrolyte. The three-electrode system was composed of a glassy carbon as the working electrode, an Ag/AgCl (saturated KCl) as the reference electrode, and a Pt wire as the counter electrode. To prepare the electrode, the slurry was mixed with the prepared samples as active materials, Ketjen black (Mitsubishi Chemical, ECP-600JD) as the conducting material, and poly(vinylidenedifluoride) (PVDF, Alfa Aesar) as the binder in the weight ratio of 7:1:2 in N-methyl–2–pyrrolidinone (NMP, 99.5%, Aldrich). The slurry was then coated on glassy carbon and dried in air at 60 °C for 1 h. In the next step, cyclic voltammetry (CV) measurements were performed in the potential range of 0.0–1.0 V at the scan rates of 10, 30, 50, 100, and 200 mV s^{-1}. In addition, the electrochemical performances of asymmetric cell constructed by activated carbon (AC) and MnO_2-PCNF3 were performed using a potentiostat/galvanostat in the 1 M Na_2SO_4 solution. The electrode of AC and MnO_2-PCNF3 were prepared by a mixed slurry of the active material (AC and MnO_2-PCNF3), the conducting material (Ketjen black, Mitsubishi chemical), and the binder (PVDF, Alfa Aesar) with the weight ratio of 7:1:2 in the NMP solvent. Prepared slurries were then casted on nickel foam as the current collector and dried at 80 °C for 10 h in a dry oven. CV and charge-discharge performance were measured at the scan rate of 10 mV s^{-1} and the current density of 0.3, 0.5, 0.7, 1.0, 1.5, 2.0, 3.0, 5.0, and 10.0 A g^{-1} in the potential rage of 0.0–2.0 V. In addition, to investigate the charge transfer and ion diffusion process, electrochemical impedance spectroscopy (EIS, PGST302N by Eco Chemie, Netherlands) for AC//MnO_2-CNF3 and AC//MnO_2-PCNF3 was measured using the fresh electrode in frequency range of 100 kHz to 10 MHz.

3. Results and discussion

Fig. 1 shows a schematic illustration of an ideal synthetic process of barnacle-like MnO_2-CNF3 and barnacle-like MnO_2-PCNF3. The conventional CNF (Fig. 1(a)) is synthesized using the PAN polymer as the carbon precursor without the SAN polymer. MnO_2-CNF3 (Fig. 1(b)) shows an agglomeration of barnacle-like MnO_2 on CNF due to the low surface area of CNF and the strong C-C bonding on the CNF surface. By contrast, PCNF (Fig. 1(c)) to obtain the porous structure of CNF is synthesized using the PAN polymer with SAN polymer as the pore forming agent. The micropores and mesopores in PCNF are formed by the decomposition of the SAN polymer during the carbonization process (see Table 1). MnO_2-PCNF3 (see Fig. 1(d)) formed the well-dispersed barnacle-like MnO_2 on the PCNF due to the high surface area of PCNF by formed pore on the surface.

Fig. 2 shows the FESEM images of MnO_2-CNF3, MnO_2-PCNF1.5, MnO_2-PCNF3, and MnO_2-PCNF7. All samples showed the diameter in the range of 274.1–432.3 nm for MnO_2-CNF3, 242.9–302.3 nm for

Table 1
BET results of specific surface area, total pore volume, pore diameter and pore size distribution for CNF and PCNF.

Samples	S_{BET} [m^2/g]	Total pore volume (p/p_0 = 0.990) [cm^3/g]	Average pore diameter [nm]	Pore size distribution	
				V_{micro} (%)	V_{meso} (%)
CNF	364.2	0.189	2.06	82.4	17.6
PCNF	816.6	0.321	2.15	58.0	42.0

MnO_2-PCNF1.5, 255.6–343.0 nm for MnO_2-PCNF3, and 301.4–421.6 nm for MnO_2-PCNF7. In addition, the PCNF in MnO_2-PCNF1.5, 3, and 7, which decomposed the SAN polymer, were found to be of smaller diameters than the conventional CNF [23]. Therefore, PCNF exhibited the high surface area (798.6 $m^2\,g^{-1}$) as compared to the conventional CNF (364.2 $m^2\,g^{-1}$). The increased surface area of PCNF plays an important role in the dispersion of barnacle-like MnO_2, leading to the enhanced electrochemical performance. In addition, the barnacle-like MnO_2 is formed on the PCNF surface by the following equation of redox reaction [24] (see Eq. (1)):

$$4MnO_4^- + 3C + H_2O = 4MnO_2 + 2HCO_3^- + CO_3^{2-} \quad (1)$$

Said differently, the barnacle-like MnO_2 is formed by the three-step process. First, Mn ion in the precursor solution forms an octahedral layer of MnO_6 combining edge-sharing. Second, octahedral layers self-assemble to the nanosheet with K^+ cations and H_2O. Finally, the barnacle-like MnO_2 is formed by the combination and growth of the MnO_2 nanosheets [25]. As shown in Fig. 2(a), due to the low surface area of CNFs, MnO_2-CNF3 showed agglomeration of barnacle-like MnO_2. Therefore, to obtain well-dispersed barnacle-like MnO_2 on the PCNF supports and to optimize the size of barnacle-like MnO_2, we controlled the different synthetic times of a chemical precipitation method: namely, for 1.5, 3, and 7 min. In the case of MnO_2-PCNF1.5 (Fig. 2(b)), barnacle-like MnO_2 with the diameter in the range of 77.9–95.2 nm were sparsely formed on the PCNF surface due to the short synthetic time. Remarkably, MnO_2-PCNF3 (Fig. 2(c)) indicated well-dispersed MnO_2 with the diameter in the range of 67–114 nm owing to the high surface area of PCNF supports. In addition, MnO_2-PCNF3 showed a larger number of barnacle-like MnO_2 on the PCNF surface than MnO_2-PCNF1.5 without the agglomeration of MnO_2. On the other hand, due to the excessive synthetic time, MnO_2-PCNF7 (see Fig. 2(d)) exhibited a large agglomeration of barnacle-like MnO_2 with the diameter in the range of 165.3–195.6 nm. As a result, due to the decreased electrochemical active sites, the large agglomeration of barnacle-like MnO_2 can reduce the electrochemical performance in PCs. Therefore, the optimized synthetic time of a chemical precipitation method was demonstrated for 3 min.

To further investigate the morphological properties of the samples, the TEM measurements were performed. Fig. 3 shows the low-resolution of MnO_2-CNF3, MnO_2-PCNF1.5, MnO_2-PCNF3, and MnO_2-PCNF7 (see Fig. 3(a)-(d)) and the high-resolution of MnO_2-CNF3, MnO_2-PCNF1.5, MnO_2-PCNF3, and MnO_2-PCNF7 (see Fig. 3(e)–(h)) TEM images, respectively. The conventional CNF displayed a uniform gray contrast, suggesting a dense morphology without pores. At the same time, PCNF exhibited the dark region with a relatively bright region on the surface owing to the pores formed by the SAN polymer. In addition, MnO_2-CNF3, MnO_2-PCNF1.5, MnO_2-PCNF3, and MnO_2-PCNF7 showed a relatively dark region on the CNF and PCNF, implying the presence of barnacle-like MnO_2. MnO_2-CNF3 (see Fig. 3(a) and (e)) showed the agglomeration of barnacle-like MnO_2 due to the low surface area of CNF, which could lead to the reduced active site with a low electrochemical performance. The barnacle-like MnO_2 in MnO_2-PCNF1.5 (see Fig. 3(b) and (f)) was sparsely located owing to the short synthetic time. Interestingly, as compared to MnO_2-PCNF1.5, MnO_2-PCNF3 (see Fig. 3(c) and (g)) showed the well-dispersed barnacle-like MnO_2 on the PCNF surface without an increase in size and agglomeration of

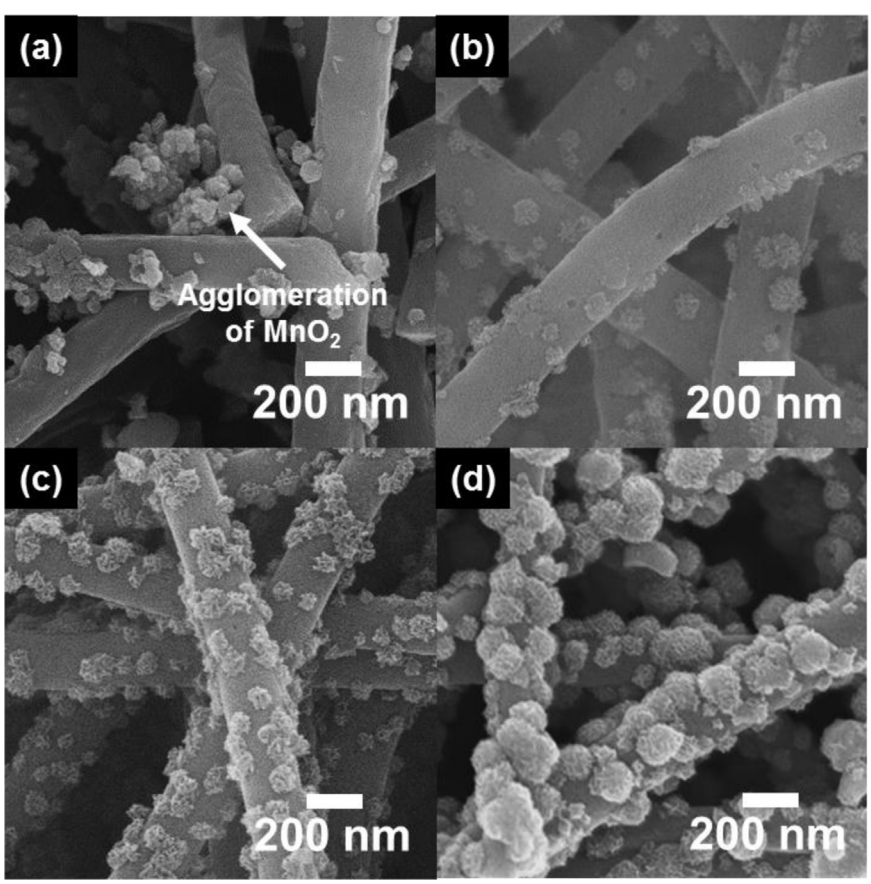

Fig. 2. The FE-SEM images of (a) MnO_2-CNF3; (b) MnO_2-PCNF1.5; (c) MnO_2-PCNF3; and (d) MnO_2-PCNF7.

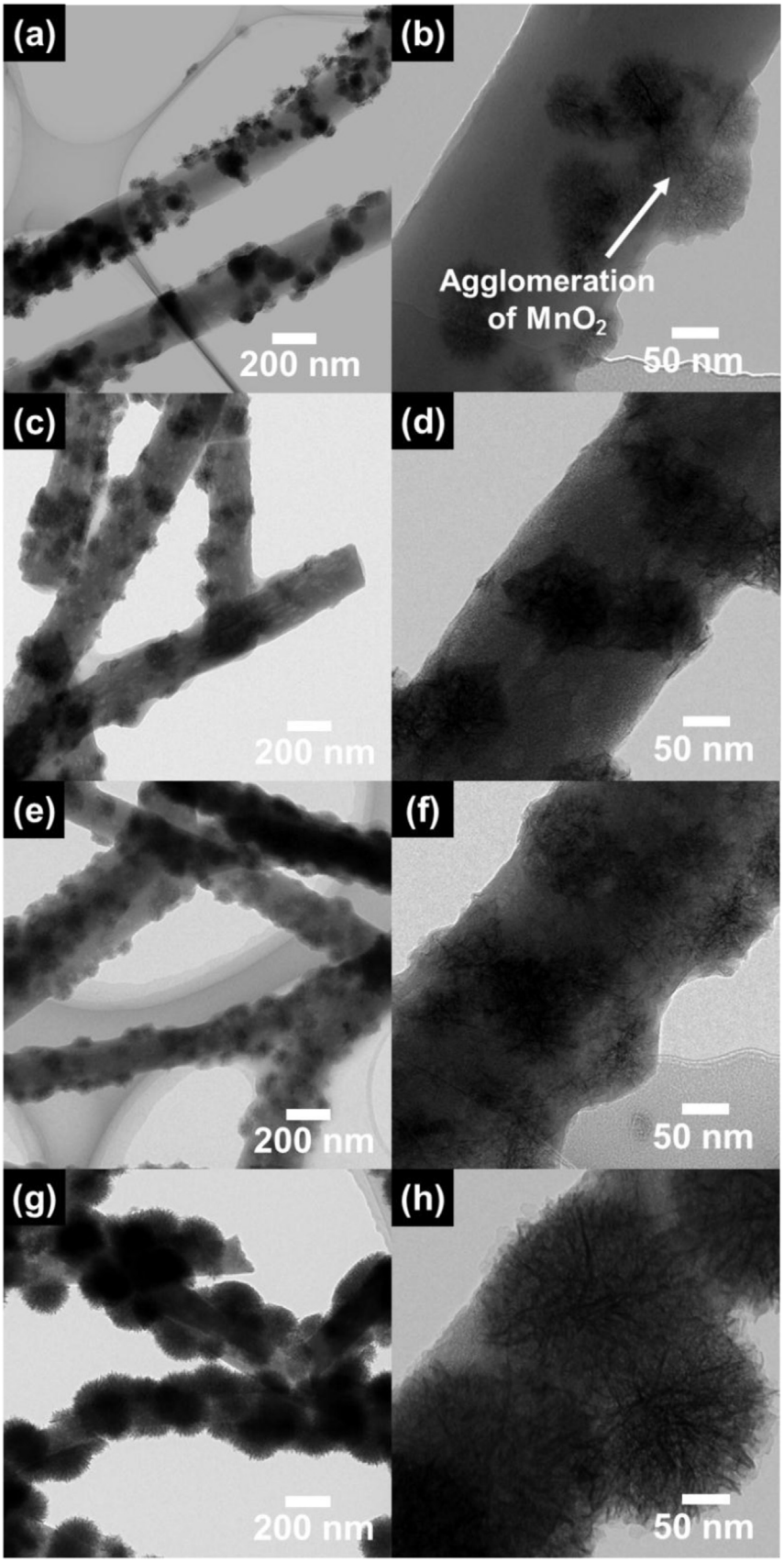

Fig. 3. The TEM images of (a) the conventional CNF, (b)-(e) a low resolution of MnO_2-CNF3, MnO_2-PCNF1.5, MnO_2-PCNF3, and MnO_2-PCNF7; (f) PCNF, and (g)-(j) high resolution of MnO_2-CNF3, MnO_2-PCNF1.5, MnO_2-PCNF3, and MnO_2/PCNF-7.

barnacle-like MnO_2. However, MnO_2-PCNF7 (see Fig. 3(d) and (h)) indicated an increased agglomeration of barnacle-like MnO_2 due to the excessive synthetic time. Therefore, due to the increased electrochemical active sites, the well-dispersed barnacle-like MnO_2 on the PCNF can provide an improved electrochemical performance [26,27].

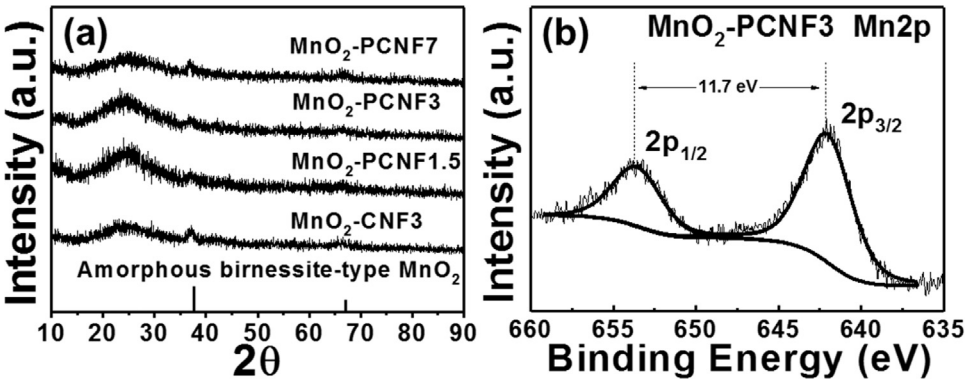

Fig. 4. (a) The XRD pattern obtained from MnO_2-CNF3, MnO_2-PCNF1.5, MnO_2-PCNF3, and MnO_2-PCNF7; (b) The XPS spectra of the Mn 2*p* obtained from MnO_2-PCNF3.

Fig. 4(a) shows the XRD patterns of MnO_2-CNF3, MnO_2-PCNF1.5, MnO_2-PCNF3, and MnO_2-PCNF7. All samples were observed a broad peak at ~ 25°, corresponding the (002) layer of graphite. In addition, in all samples, two main characteristic peaks were observed at 37.1° and 66.3°, corresponding to the (006) and (119), respectively. The XRD patterns were in good agreement with birnessite-type MnO_2 structure (space group C2/m; JCPDS card No. 18–0802) [28]. Therefore, barnacle-like MnO_2 coated PCNF consists of birnessite-type MnO_2 nanoparticles and amorphous PCNF supports. To further investigate the chemical bonding states, the XPS measurements were performed for MnO_2-PCNF3 (see Fig. 4(b)). The Mn 2p core-level spectra exhibited two different signals at ~ 654.1 eV and ~ 642.4 eV, corresponding to the Mn $2p_{1/2}$ and Mn $2p_{3/2}$ photoelectrons of the MnO_2 phase (Mn^{4+}), respectively [29]. Moreover, the energy separation between the Mn $2p_{1/2}$ and Mn $2p_{3/2}$ peaks was ~ 11.7 eV, which was in a good agreement with a MnO_2 structure [30,31]. This result means that the MnO_2 phases were well-formed on the PCNF surface by a chemical precipitation method for 3 min.

Fig. 5(a)-(d) shows the cyclic voltammograms (CVs) of all samples using the three-electrode system in the 0.5 M H_2SO_4 electrolyte. All samples were performed at the scan rates of 10, 30, 50, 100, and 200 mV s^{-1} in the potential range of 0.0–1.0 V (vs. Ag/AgCl). The CV curves of all samples shows the electrochemical behavior around 0.4 V owing to the Faradaic redox reaction of MnO_2. The Faradaic redox reaction mechanism of MnO_2 in electrolyte can be associated by following equation [32] (see Eq. (2)):

$$MnO_2 + A^+ + e^- \leftrightarrow MnOOA^+ \quad (2)$$

where A^+ is protons (H_3O^+) or alkali metal ions, such as Na^+, Li^+, and K^+ in electrolyte. MnO_2-PCNF3 electrode displays the largest curve area as compared to other electrodes, indicating an improved electrochemical property by increased active sites between the electrode and the electrolyte. The specific capacitance of the electrodes was evaluated using the following equation [33,34] (see Eq. (3)):

$$C = ((q_a + q_c)/2m\Delta V) \quad (3)$$

where q_a and q_c are the charges of anodic and cathodic areas integrated in the CVs, whereas m and ΔV are mass of the active materials and the potential range of the CVs, respectively. The specific capacitance of MnO_2-CNF3, MnO_2-PCNF1.5, MnO_2-PCNF3, and MnO_2-PCNF7 electrodes were ~ 160.4, ~ 142.9, ~ 209.8, and ~ 175.1 F g^{-1} at 10 mV s^{-1}, respectively. MnO_2-PCNF3 shows × 1.31, 1.47, and 1.20

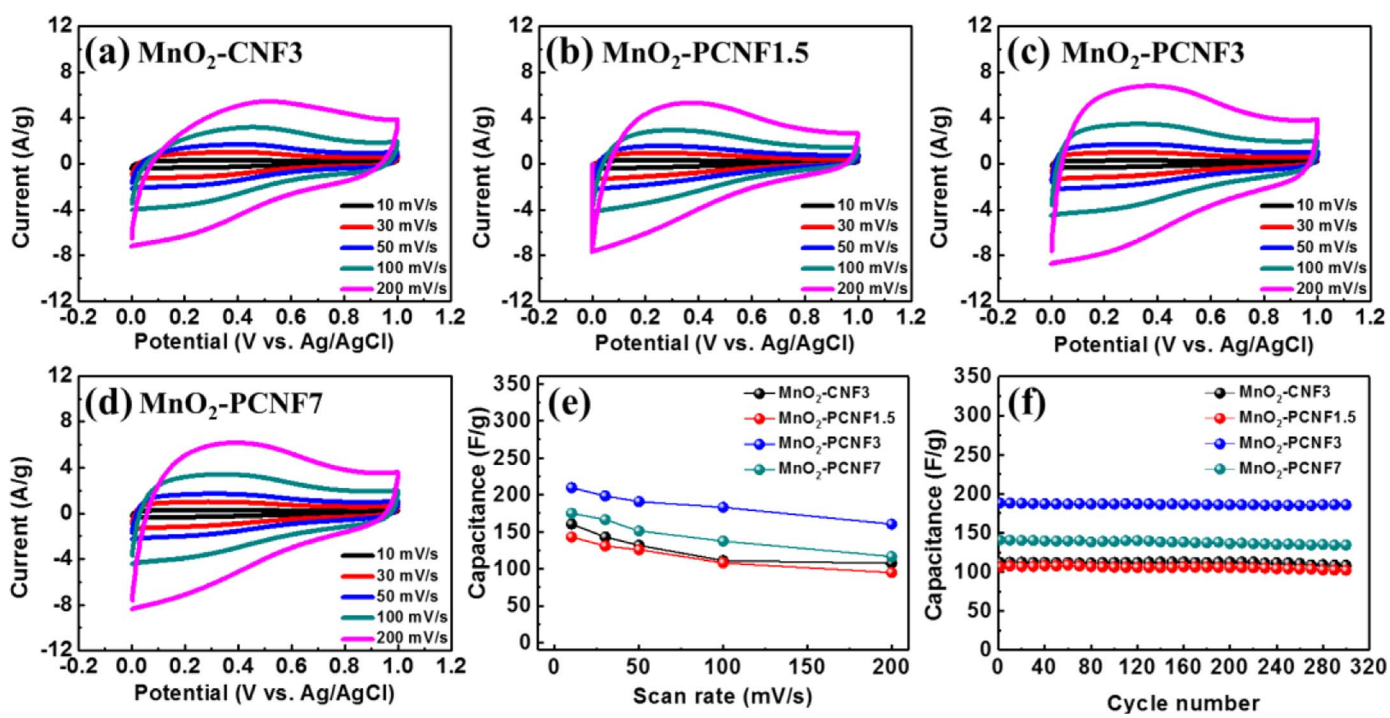

Fig. 5. Cyclic voltammetry (CV) measurement obtained from (a) MnO_2-CNF3; (b) MnO_2-PCNF1.5; (c) MnO_2-PCNF3; and (d) MnO_2-PCNF7 evaluated using a conventional three-electrode system at the scan rate of 10, 30, 50, 100, 200 mV s^{-1} in the potential range of 0.0–1.0 V (vs. Ag/AgCl). (e) The capacitance estimated as a function of a potential scan rate; (f) The cycling stability obtained from all samples.

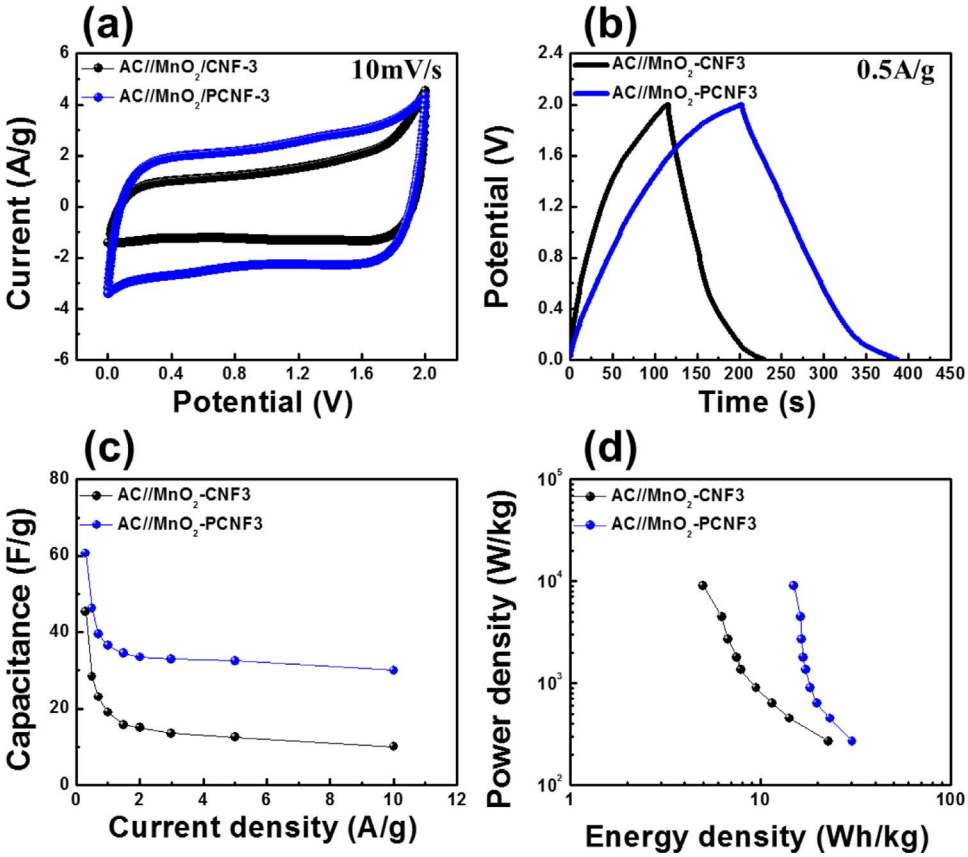

Fig. 6. (a) Cyclic voltammetry (CV) curves at the scan-rate of 10 mV s^{-1}; (b) galvanostatic charge/discharge curves at current density of 0.5 A g^{-1}, (c) the specific capacitance by varying the current density to 0.3–10.0 A g^{-1}; and (d) Ragone plots obtained from asymmetric cell constructed activated carbon (AC) and MnO_2-CNF3 (AC//MnO_2-CNF3), AC and MnO_2-PCNF3 (AC//MnO_2-PCNF3).

times higher than the MnO_2-CNF3, MnO_2-PCNF1.5, and MnO_2-PCNF7, respectively. These results mean that the improved capacitance can be attributed to the increased active site between the well-dispersed barnacle-like MnO_2 and the electrolyte. Fig. 5(e) shows the specific capacitance of all samples at the scan rates of 10, 30, 50, 100, and 200 mV s^{-1}. Due to the limited ion diffusion in the electrolyte, the specific capacitances of all samples decrease with an increasing scan rate. That is, MnO_2-CNF3, MnO_2-PCNF1.5, MnO_2-PCNF3, and MnO_2-PCNF7 showed the capacitances of ~ 107.5, ~ 95.1, ~ 160.3, and ~ 116.5 F g^{-1} at 200 mV s^{-1}, respectively. The capacitance retentions of all samples were 67.1%, 66.5%, 76.4%, and 66.4%, respectively. Of note, due to the good dispersion of barnacle-like MnO_2, MnO_2-PCNF3 showed a superior high-rate performance as compared to the other samples. Thus, the improved dispersion of barnacle-like MnO_2 could provide a rapid ion diffusion rate, leading to a high-rate performance. Fig. 5(f) indicates the cycling stability of all samples up to 300 cycles at the scan rate of 100 mV s^{-1}. The cycling stability of MnO_2-CNF3, MnO_2-PCNF1.5, MnO_2-PCNF3, and MnO_2-PCNF7 were 96.6%, 95.8%, 98.7%, and 95.5%, respectively.

Fig. 6(a) shows the CV curves of asymmetric cell constructed AC and MnO_2-CNF3, AC and MnO_2-PCNF3. The CV curves were measured at the scan rate of 10 mV s^{-1} with the potential range of 0.0–2.0 V in 1 M Na_2SO_4 solution. The MnO_2-PCNF3 shows the higher peak and a larger CV area, indicating a larger electrochemical performance than MnO_2-CNF3. Fig. 6(b) indicates the galvanostatic charge/discharge curve of the asymmetric cell at 0.5 A g^{-1} in the potential range 0.0–2.0. The discharge times of samples were observed to be 115 s for AC//MnO_2-CNF3 and 185 s for AC//MnO_2-PCNF3, meaning that AC//MnO_2-PCNF3 exhibits a higher capacitance behavior than AC//MnO_2-CNF3 at the current density of 0.5 A g^{-1}. Fig. 6(c) shows the specific capacitance of the AC//MnO_2-CNF3 and AC//MnO_2-PCNF3. The specific capacitance is calculated form the following equation [35] (see Eq. (4)):

$$C_{sp} = I\Delta t/m\Delta V \tag{4}$$

where C_{sp} is the specific capacitance (F g^{-1}), Δt is the total discharge time (s), I is the current (A), m is the mass of active material (g), and Δv is the potential range. The specific capacitance of AC//MnO_2-CNF3 and AC//MnO_2-PCNF3 at the current density of 0.3 A g^{-1} were ~ 45.3 F g^{-1} and ~ 60.6 F g^{-1}. Specifically, at the high current density of 10.0 A g^{-1}, owing to the good dispersion of barnacle-like MnO_2 nanoparticles, AC//MnO_2-PCNF3 had a higher capacitance (~ 33.0 F g^{-1}) than AC//MnO_2-CNF3 (~ 10.0 F g^{-1}). Fig. 6(d) shows a Ragone plot calculated using Eq. (5) [36].

$$E = [0.5C_{sp}(\Delta V)^2]/3.6$$
$$P = 3.6\,E/\Delta t \tag{5}$$

where C_{sp} is the specific capacitance of samples (F g^{-1}), ΔV is potential range excluding the initial drop (V), and Δt is the total discharge time (s). The Ragon plots are indicated by varying the current density to 0.3, 0.5, 0.7, 1.0, 1.5, 2.0, 3.0, 5.0, and 10.0 A g^{-1}. The energy density of AC//MnO_2-CNF3 and AC//MnO_2-PCNF3 shows the 45.3–10.0 Wh kg^{-1} and 60.6–30.0 Wh kg^{-1} over the power density range of 270–9000 W kg^{-1}, respectively.

To investigate the electrochemical kinetics of AC//MnO_2-CNF3 and AC//MnO_2-PCNF3, EIS test was performed. Fig. 7 shows the Nyquist plots of AC//MnO_2-CNF3 and AC//MnO_2-PCNF3. The semicircle in the high-frequency region is attributed to the charge-transfer resistance (R_{ct}) at the electrode-electrolyte interface, and the straight line in the low-frequency region (the Warburg impedance) corresponds to ion diffusion in the electrode. In the high-frequency region, a smaller semicircle means the lower charge-transfer resistance. Thus, the AC//MnO_2-PCNF3 exhibits lower charge-transfer resistance and lower Warburg impedance compared with the AC//MnO_2-CNF3 due to the unique structure of well-dispersed barnacle-like MnO_2 nanoparticles, indicating the high number of electroactive sites between MnO_2 and electrolyte and a shorter length of ion diffusion.

The excellent electrochemical performance of MnO_2-PCNF3 can be

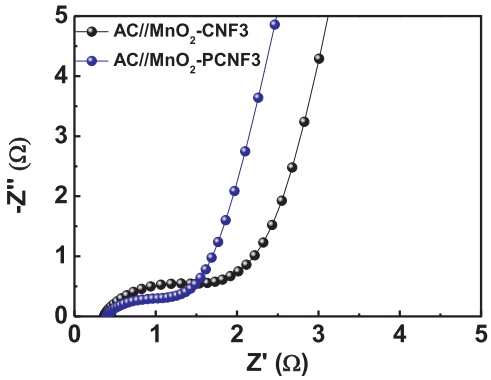

Fig. 7. EIS results of the AC//MnO_2-CNF3 and AC//MnO_2-PCNF3 asymmetric cells.

explained by the following two main effects: (1) barnacle-like MnO_2 nanoparticles with a high active area relative to the increased specific capacitance; (2) good dispersion of MnO_2 nanoparticles having a short ion diffusion length on PCNF relative to a superior high-rate performance. These results suggest that MnO_2-PCNF3 is a promising candidate as the electrode material for high-performance PCs.

4. Conclusions

In the present study, MnO_2-PCNF was synthesized using electrospinning and the chemical precipitation method. To obtain the well-dispersed barnacle-like MnO_2, the PCNF was prepared using the decomposition of the SAN polymer during the carbonization process. In addition, the synthetic time of a chemical precipitation method for 1.5, 3, and 7 min was controlled to obtain the improved dispersion and the optimum size of barnacle-like MnO_2 on the PCNF supports. As a result, MnO_2-PCNF3 exhibited the unique nanoarchitecture with the well-dispersed barnacle-like MnO_2 decorated on the PCNF supports. The optimized MnO_2-PCNF3 also showed the improved specific capacitance of 209.8 F g^{-1} at the scan rate of 10 mV s^{-1}, as well as the superior high-rate performance and capacitance retention of 98.7% as compared to MnO_2-CNF3, MnO_2-PCNF1.5, and MnO_2-PCNF7. Specifically, electrochemical performances of asymmetric cell of AC//MnO_2-PCNF3 indicated the high capacitance (60.6–30.0 F g^{-1} in current density of from 0.5 to 10 A g^{-1}) and excellent energy density (30.3–15.0 Wh kg^{-1} with power density of 270–9000 W kg^{-1}). The enhanced electrochemical performance can be explained by two major effects. First, a high specific capacitance can be attributed to the formation of barnacle-like MnO_2 nanoparticles with a high active area. Second, the superior high-rate performance can be ascribed to the well-dispersed MnO_2 nanoparticles on PCNF with a short ion diffusion length. Thus, MnO_2-PCNF3 has a great potential for use in high-performance PCs.

Acknowledgement

This work was supported by the Industrial Fundamental Technology Development Program (10052745, Development of nano-sized (100 nm) manganese ceramic material for high voltage pseudo-capacitor) funded by the Ministry of Trade, Industry and Energy (MOTIE) of Korea.

References

[1] T. Tomai, S. Mitani, D. Komatsu, Y. Kawaguchi, I. Honma, Metal-free aqueous redox capacitor via proton rocking-chair system in an organic-based couple, Sci. Rep. 4 (2014) 3591.
[2] T. Hibino, K. Kobayashi, M. Nagao, S. Kawasaki, High-temperature supercapacitor with a proton-conducting metal pyrophosphate electrolyte, Sci. Rep. 5 (2015) 7903.
[3] G.-H. An, H.-J. Ahn, W.-K. Hong, Electrochemical properties for high surface area and improved electrical conductivity of platinum-embedded porous carbon nanofibers, J. Power Sources 274 (2015) 536–541.
[4] J. Zhang, J.P. Cheng, M. Li, L. Liu, F. Liu, X.B. Zhang, Flower-like nickel-cobalt binary hydroxides with high specific capacitance: tuning the composition and asymmetric capacitor application, J. Electroanal. Chem. 743 (2015) 38–45.
[5] E. Lust, A. Janes, M. Arulepp, Influence of solvent nature on the electrochemical parameters of electrical double layer capacitors, J. Electroanal. Chem. 562 (2004) 33–42.
[6] S.-E. Chun, B. Evanko, X. Wang, D. Vonlanthen, X. Ji, G.D. Stucky, S.W. Boettcher, Design of aqueous redox-enhanced electrochemical capacitors with high specific energies and slow self-discharge, Nat. Commun. 6 (2015) 7818.
[7] H.B. Li, M.H. Yu, F.X. Wang, P. Liu, Y. Liang, J. Xiao, C.X. Wang, Y.X. Tong, G.W. Yang, Amorphous nickel hydroxide nanospheres with ultrahigh capacitance and energy density as electorchemical pseudocapacitor materials, Nat. Commun. 4 (2013) 1894.
[8] V. Venkatachalam, A. Alsalme, A. Alghamdi, R. Jayavel, High performance electrochemical capacitor based on $MnCo_2O_4$ nanostructured electrode, J. Electroanal. Chem. 756 (2015) 94–100.
[9] J. Cao, Y. Wang, Y. Zhou, D. Jia, J.H. Ouyang, L. Guo, Performances of high voltage electrochemical capacitor using ball-milled graphite/Mn_3O_4 composite electrodes, J. Electroanal. Chem. 682 (2012) 23–28.
[10] G. Yuan, Y. Liu, M. Yue, H. Li, E. Liu, Y. Huang, D. Kong, Cu-doped NiO for aqueous asymmetric electrochemical capacitors, Ceram. Int. 40 (2014) 9101–9105.
[11] X. Zhao, L. Zhang, S. Murali, M.D. Stoller, Q. Zhang, Y. Zhu, R.S. Ruoff, Incorporation of manganese dioxide within ultraporous activated graphene for high-performance electrochemical capacitors, ACS Nano 6 (2012) 5404–5412.
[12] G.-H. An, J.I. Sohn, H.-J. Ahn, Hierarchical architecture of hybrid carbon-encapsulated hollow manganese oxide nanotubes with a porous-wall structure for high-performance electrochemical energy storage, J. Mater. Chem. A 4 (2016) 2049–2054.
[13] S. Hong, S. Lee, U. Paik, Core-shell tubular nanostructured electrode of hollow carbon nanofiber/manganese oxide for electrochemical capacitors, Electrochim. Acta 141 (2014) 39–44.
[14] D. Qu, H. Shi, Studies of activated carbons used in double-layer capacitors, J. Power Sources 74 (1998) 99–107.
[15] D.L. Castello, D.C. Amoros, A.L. Solano, S. Shiraishi, H. Kurihara, A. Oya, Influence of pore structure and surface chemistry on electric double layer capacitance in non-aqueous electrolyte, Carbon 41 (2003) 1765–1775.
[16] G.-H. An, H.-J. Ahn, Surface modification of RuO_2 nanoparticles-carbon nanofiber composites for electrochemical capacitors, J. Electroanal. Chem. 744 (2015) 32–36.
[17] D. Pan, M. Ombaba, Z.-Y. Zhou, Y. Liu, S. Chen, J. Lu, Direct growth of carbon nanofibers to generate a 3D porous platform on a metal contact to enable an oxygen reduction reaction, ACS Nano 6 (2012) 10720–10726.
[18] M.K.V. Lee, A.J.V. Dilllen, J.H. Bitter, K.P.D. Jong, Deposition precipitation for the preparation of carbon nanofiber supported nickel catalysts, J. Am. Chem. Soc. 127 (2005) 13573–13582.
[19] G.-H. An, H.-J. Ahn, Activated porous carbon nanofibers using Sn segregation for high-performance electrochemical capacitors, Carbon 65 (2013) 87–96.
[20] G.-H. An, E.-H. Lee, H.-J. Ahn, Well-dispersed iron nanoparticles exposed within nitrogen-doped mesoporous carbon nanofibers by hydrogen-activation for oxygen reduction reaction, J. Alloy. Compd. 682 (2016) 746–752.
[21] M. Zhi, A. Manivannan, F. Meng, N. Wu, Highly conductive electrospun carbon nanofiber/MnO_2 coaxial nano-cables high energy and power density supercapacitors, J. Power Sources 208 (2012) 345–353.
[22] Y.-G. Lee, G.-H. An, H.-J. Ahn, Improved mesoporous structure of high surface area carbon nanofiber for electrical double-layer capacitors, Korean J. Mater. Res. 27 (2017) 192–198.
[23] B.-S. Lee, S.-B. Son, K.-M. Park, G. Lee, K.H. Oh, S.-H. Lee, W.-R. Yu, Effect of pores in hollow carbon nanofibers on their negative electrode properties for a lithium rechargeable battery, ACS Appl. Mater. Interfaces 4 (2012) 6702–6710.
[24] Y. Luo, J. Jiang, W. Zhou, H. Yang, J. Luo, X. Qi, H. Zhang, D.Y.W. Yu, C.M. Li, T. Yu, Self-assembly of well-ordered whisker-like manganese oxide arrays on carbon fiber paper and its application as electrode material for supercapacitors, J. Mater. Chem. 22 (2012) 8634–8640.
[25] D. Yan, P.X. Yan, G.H. Yue, J.Z. Liu, J.B. Chang, Q. Yang, D.M. Qu, Z.R. Geng, J.T. Chen, G.A. Zhang, R.F. Zhuo, Self-assembled flower-like hierarchical spheres and nanobelts of manganese oxide by hydrothermal method and morphology control of them, Chem. Phys. Lett. 440 (2007) 134–138.
[26] J. Yan, Z. Fan, T. Wei, W. Qian, M. Zhang, F. Wei, Fast and reversible surface redox reaction of graphene-MnO_2 composites as supercapacitor electrodes, Carbon 48 (2010) 3825–3833.
[27] M. Liu, L. Gan, W. Xiong, Z. Xu, D. Zhu, L. Chen, Development of MnO_2/porous carbon microspheres with a partially graphitic structure for high performance supercapacitor electrodes, J. Mater. Chem. A 2 (2014) 2555–2562.
[28] J.-G. Wang, Y. Yang, Z.-H. Huang, F. Kang, Coaxial carbon nanofibers/MnO_2 nanocomposites as freestanding electrodes for high-performance electrochemical capacitors, Electrochim. Acta 56 (2011) 9240–9247.
[29] M.A. Stranick, MnO_2 by XPS, Surf. Sci. Spectra 6 (1999) 31–38.
[30] M. Xue, L. Huang, J.-Q. Wang, Y. Wang, L. Gao, J.-H. Zhu, Z.-G. Zou, The direct synthesis of mesoporous structured MnO_2/TiO_2 nanocomposite: a novel visible-light active photocatalyst with large pore size, Nanotechnology 19 (2008) 185604–185612.
[31] Z. Lei, J. Zhang, X.S. Zhao, Ultrathin MnO_2 nanofibers grown on graphitic carbon spheres as high-performance asymmetric supercapacitor electrodes, J. Mater. Chem. 22 (2012) 153–160.
[32] J.W. Long, C.P. Rhodes, A.L. Young, D.R. Rolison, Ultrathin, protective coating of poly(o-phenylenediamine) as electrochemical proton gates: making mesoporous MnO_2 nanoarchitectures stable in acid electrolytes, Nano Lett. 3 (2003) 1155–1161.

[33] M. Liu, W.W. Tjiu, J. Pan, C. Zhang, W. Gao, T. Liu, One-step synthesis of graphene nanoribbon-MnO_2 hybrids and their all-solid-state asymmetric supercapacitors, Nanoscale 6 (2014) 4233–4242.
[34] X. Li, W. Xing, S. Zhuo, J. Zhou, F. Li, S.-Z. Qiao, G.-Q. Lu, Prepartion of capacitor's electrode from sunflower seed shell, Bioresour. Technol. 102 (2011) 1118–1123.
[35] Y. Jin, H. Chen, M. Chen, N. Liu, Q. Li, Graphene-patched CNT/MnO_2 nanocomposite papers for the electrode of high-performance flexible asymmetric supercapacitors, ACS Appl. Mater. Interfaces 5 (2013) 3408–3416.
[36] D.-Y. Sin, I.-K. Park, H.-J. Ahn, Enhanced electrochemical performance of phosphorus incorporated carbon nanofibers by the spin-on dopant method, RSC Adv. 6 (2016) 58823.